Ground Water Induced Changes in Velocities of P and S Waves (Vp and Vs) Measured Using Accurately Controlled Seismic Source

Rina Suzuki (suzurina@seis.nagoya-u.ac.jp)
Nagoya University
Koshun Yamaoka
Nagoya University: Nagoya Daigaku
Shuhei Tsuji
Nagoya University: Nagoya Daigaku
Toshiki Watanabe
Nagoya University: Nagoya Daigaku

Full paper

Keywords: Seismic velocity change, artificial seismic source, ACROSS, fluid saturation, ground water level

Posted Date: December 30th, 2020

DOI: https://doi.org/10.21203/rs.3.rs-136036/v1

Version of Record: A version of this preprint was published at Earth, Planets and Space on July 28th, 2021. See the published version at https://doi.org/10.1186/s40623-021-01484-3.

Title: Ground water induced changes in velocities of P and S waves (Vp and Vs) measured using accurately controlled seismic source

Author #1: Rina Suzuki, Graduate School of Environmental Studies, Nagoya University; suzurina@seis.nagoya-u.ac.jp

Author #2: Koshun Yamaoka, Graduate School of Environmental Studies, Nagoya University; kyamaoka@seis.nagoya-u.ac.jp

Author #3: Shuhei Tsuji, Graduate School of Environmental Studies, Nagoya University; stsuji@seis.nagoya-u.ac.jp

Author #4: Toshiki Watanabe, Graduate School of Environmental Studies, Nagoya University; watanabe@seis.nagoya-u.ac.jp

Abstract

We analyzed the temporal variation in the travel times of both the P and S waves (Vp and Vs) for 14 months at Toyohashi (central Japan) with a continuously operating vibration source that could produce both P and S waves efficiently. The seismic waves produced by the source, which is named ACROSS (accurately-controlled routinely-operated signal system), were recorded by three nearby seismic stations, and the travel time variation at each station was calculated using the transfer function calculated from the recorded data. We observed the seasonal variations in the Vp and Vs for all the stations—which can be interpreted using the change in the fluid saturation and crack density of subsurface rocks—are consistent with the variation in the ground water level. The short-term responses to rainfall are observed at the nearest station; the interpretation of the changes in crack density and saturation is inconsistent with the ground water observation partly due the initial response to rainfall. This can be interpreted as an air-water mixture within pores or cracks on a fine scale.

Keywords

27 Seismic velocity change, artificial seismic source, ACROSS, fluid saturation; ground
28 water level

29 Main Text

30 1 Introduction

31 Changes in atmospheric conditions, such as rainfall and air temperature, results in
32 changes in seismic velocity, and many studies have been conducted on the effects of other
33 factors and their impact on seismic velocity. Rainfalls are the most effective source of
34 seismic velocity changes because they result in the direct infiltration of water to fill the
35 pores of the subsurface soil or rock (Martini et al. 2009). Changes in air temperature have
36 recently been found to influence subsurface seismic velocity (Richter et al. 2014; Wang
37 et al. 2019), which may be difficult to understand considering the penetration depth of the
38 atmospheric temperature variation. However, seasonal velocity changes are generally
39 observed in relation to ground water level variation (Sens-Schönfelder and Wegler 2006;
40 Clements and Denolle 2018). In addition to atmospheric conditions, strong earthquakes
41 also affect seismic velocity (Niu et al. 2008; Nakata and Snieder 2011). This was initially
42 found by Ikuta et al. (2002) and is now a well-known phenomenon.

43 The seismic velocity of the subsurface medium changes with the variations in the
44 rock conditions, such as an increase or decrease in the cracks or fluids within the rocks.
45 Nur and Simmons (1969) found that the velocity change is the seismic waves as a function
46 of the pressure of dry and saturated rocks through laboratory experiments. King et al.
47 (2000) also investigated the velocity change with the increasing saturation using
48 laboratory experiments. The results of both the studies show that the effect of fluids on
49 seismic velocity differs for the P and S waves. O'Connell and Budiansky (1974)
50 theoretically proved that the seismic velocity depends on the spatial density and fluid
51 saturation ratio of the cracks in the subsurface rocks. Their results showed that the P wave
52 velocity (Vp) and S wave velocity (Vs) differ in terms of their dependence on the cracks
53 and fluids in the subsurface rocks; therefore, the state of cracks and fluid within the
54 subsurface medium can be evaluated using the Vp and Vs variations.

55 To observe the temporal variation of seismic velocity, both natural and artificial
56 sources were used. Natural sources, such as ambient noise, are now commonly used in
57 combination with seismic interferometry (SI) (Brenguier et al. 2008; Liu et al. 2014;
58 Hobiger et al. 2016). Seismic interferometry is also applied to the coda waves (Grêt et al.

59 2006) or shear waves (Miao et al. 2018) of natural earthquakes for detecting seismic wave
60 velocity changes. Artificial sources, such as vibroseis (Karageorgi et al. 1992),
61 piezoelectric actuators (Yamamura et al. 2003; Silver et al. 2007), and seismic airguns
62 (Wegler et al. 2006; Wang et al. 2019), are also used to study the temporal variation of
63 seismic velocity with high resolution.

64 In our study, an artificial seismic source called ACROSS (accurately-controlled
65 routinely-operated signal system) is used to monitor the temporal variations in the seismic
66 velocities of the P and S waves. It generates vibrations by precisely controlling the
67 rotation of the eccentric weights. Because this source has high temporal stability and,
68 therefore, can obtain a high signal-to-noise ratio (SNR) by stacking, it has the advantage
69 of continuous and high-resolution monitoring of the velocity variations (Yamaoka et al.
70 2001). Ikuta et al. (2002) and Ikuta and Yamaoka (2004) monitored the travel time
71 variation for 15 months near the fault that caused the Kobe earthquake in 1995 and
72 detected changes due to strong ground motion owing to earthquakes. Saiga et al. (2006)
73 analyzed one-month long records to show that the signal was sensitive to temperature
74 variations and rainfall. Additionally, Maeda et al. (2015) found a difference in the transfer

functions between the active and inactive periods of the Sakurajima Volcano, Japan. Furthermore, Tsuji et al. (2018) detected the coseismic and secular changes in the Tokai region by examining the travel time variations for a period of 10 years.

In this study, we measured the travel time variations of both the P and S waves by taking advantage of a new type of ACROSS source and interpreted the variation by obtaining a response to the fluid and cracks within the subsurface medium. The new type of ACROSS source (see Figure 1) has a horizontal rotation axis to produce both vertical and horizontal forces in contrast to conventional ACROSS sources that have a vertical rotation axis. Therefore, the new type of ACROSS source effectively excites both the P and S waves. The source was deployed at an observatory of the Nagoya University in March 2014 and started continuous operation at the end of 2017 after the performance tests. In this study, we analyze the signal from the continuous operation of ACROSS to monitor the travel time variations of both the P and S waves and discuss the influence of rainfall and groundwater level on the observed variations.

2 Source and data

We monitored the travel time variations of the P and S waves from December 8, 2017

to February 7, 2019 using the signal from the ACROSS observed at three seismic stations located around the source. We also compared the change in the travel time with the rainfall and ground-water level data to interpret the origin of the temporal change in the seismic velocity. In this section, we briefly overview the ACROSS source and experiment site used in our study.

2.1. Location of ACROSS (accurately-controlled routinely-operated signal system) source and observation stations

The locations of the ACROSS source and observation stations used in this study are shown in Figure 2. The ACROSS source was installed in the Mikawa Observatory of the Nagoya University in Toyohashi city (central part of Japan). The seismic signal generated by the ACROSS source was monitored by three observation stations named NU.MIK (Mikawa), N.THNH (Toyohashikita), and N.MKBH (Mikkabi). NU.MIK is located in a vault of the Mikawa Observatory and equipped with a Streckeisen STS-2 seismometer, which is a three-component broadband velocity-type sensor; the distance of the station from the source is 170 m. N.THNH and N.MKBH belong to the Hi-net stations (National

Research Institute for Earth Science and Disaster Resilience 2019) and are equipped with short-period velocity sensors in boreholes of 203 m and 103 m, respectively. The distances from the source to the N.THNH and N.MKBH stations are 3.4 km and 6.0 km, respectively. We used the rainfall data from the automated meteorological data acquisition system (AMeDAS) of the Toyohashi and Mikkabi stations operated by the Japan Meteorological Agency (JMA). The ground water levels were observed at three sites called TYH1, TYH2, and TYE, which were located adjacent to the source (Figure 2) by the National Institute of Advanced Industrial Science and Technology (AIST). The TYH2 station sampled the water pressure at a depth of 130–150 m, and the THY1 and TYE stations sampled the water pressure between 180 m and 200 m. The details of this observation are summarized in Matsumoto et al. (2007).

2.2. Signal generation using accurately-controlled routinely-operated signal system (ACROSS) source

ACROSS sources generate sinusoidal waves of various frequencies by rotating the eccentric weights. Frequency modulations (FM) are applied to the rotation to generate

123 signals in a certain width of the frequency band. As the frequency modulations are
124 repeated in a precise constant time interval (FM period), the generated signal is expressed
125 by a sum of sinusoids, whose frequencies are integer multiples of the reciprocal of the
126 FM period.

127 We used an FM period of 50 s, with an upsweep of 37.5 s and downsweep of 12.5 s.
128 The modulation frequency was centered at 10.005 Hz and ranged from 5 Hz to 15 Hz.
129 Therefore, this modulation produces sinusoidal signals at 10.005 Hz $\pm$ 0.02, 0,04, 0.06
130 … Hz between approximately 5 and 15 Hz. The source switches its rotation direction
131 every 2 h to synthesize two perpendicular linear forces after the data acquisition is
132 completed. As the eccentric weight of the ACROSS source rotates around the horizontal
133 axis, we can synthesize both the vertical and horizontal linear forces that orient
134 perpendicular to the rotation axis. The P and S waves can thus, be efficiently excited using
135 the vertical and horizontal linear forces that can be separated by this operation. Technical
136 details of the analysis method can be found in the textbook by Kasahara and Hasada
137 (2016).

138

2.3. Availability of data

Before analysis, we removed the data that were unusable due to troubles with the source or seismic stations. We first picked out the days when the ACROSS vibrator was not working correctly by looking at the operation logs of the source acquired every second. Further, we compared the logs of the rotation frequencies and angular position of the eccentric weights with those in the period that we considered the ACROSS stably operated. We chose the day of reference as June 17, 2018, and removed the days that included mean deviations of more than 0.001 % for frequency deviation and 0.12 % for angular position. As a result, we could remove the days when the source was under maintenance or stopped because of power outages. In addition to the problems in the source operation, we selected the days that indicated disorders in the seismographs. Further, sensor check signals included in the data of the Hi-net stations (N.THNH and N.MKBH) were used to find sensor disorders using the method described by Kunitomo (2014). We calculated the cross-correlation of the sensor check signal by referring to data obtained on December 1, 2017. The reference signal was chosen from the period that showed a stable cross-correlation. Data having a cross-correlation coefficient of less than

155 0.8 were excluded. For the NU.MIK station, which did not have a sensor-check signal,
156 we assumed that no trouble originated in the sensor itself because a feed-back type sensor
157 (STS-2 seismometer) was deployed in the vault. The usable days of the UD (up-down),
158 NS (north-south), and EW (east-west) components of each observation station are shown
159 in Table 1. Finally, 87 % of the data obtained during the monitoring period could be used
160 in our study, excluding the NS component of the N.MKBH station, which mostly suffered
161 from sensor trouble.

162

163 Table 1 Results of data screening based on operation normality of ACROSS source and
164 seismic stations.

(a)	Usable data	Unusable data
ACROSS source	375	52

(b)	UD component	NS component	EW component
NU.MIK	361	361	361

N.THNH	375	375	375
N.MKBH	373	279	374

(a) show usable and unusable days because of ACROSS source. (b) show number of available days for each component out of usable days in (a).

3 Data processing

We calculated the travel time variations from the transfer functions between the observed waveforms at the seismic stations and the source function of the ACROSS vibrator. The transfer functions were calculated based on the standard procedure described by Kasahara and Hasada (2016). The travel time variations were calculated using the method described by Ikuta et al. (2002). In this study, we briefly explain the data processing to obtain the travel time variations for both the P and S waves, along with data stacking and transfer function calculation.

3.1. Stacking of observation data

We made the stacking of the observed waves to enhance the SNR and improve the detectability of the temporal variation in the travel time. In the stacking, we use the weighted stack method proposed by Nagao et al. (2010), as shown in the following equations:

$$X_s(f) = \sum_{k=1}^{K} w(f,k)X(f,k) \tag{1}$$

$$w(f,k) = \varepsilon(f,k)^{-2} \Big/ \sum_{k'=1}^{K} \varepsilon(f,k')^{-2} \tag{2}$$

$$\varepsilon_s(f) = \sqrt{1 \Big/ \sum_{k=1}^{K} \varepsilon(f,k)^{-2}} \tag{3}$$

Equation (1) gives the stacked data $[X_s(f)]$ using a weight $[w(f,k)]$ for the *k*-th day's data $[X(f,k)]$ at the frequency (f). *K* is number of usable dates for the analysis. The weight is given by the noise variance $[\varepsilon(f,k)^2]$ as shown in equation (2). Stacking is performed on the data of every 400-seconds long section. As each section includes eight cycles of frequency modulation, the signal of the ACROSS source appears after every

187 eight components in the frequency series; and therefore, other components include only
188 noise. The noise variance is assumed to be equivalent to the squared amplitude of the
189 frequency component adjacent to the component of the ACROSS signal. $\varepsilon_s(f)$ in
190 equation (3), which is the noise level after stacking, is used in the following analysis to
191 obtain the estimation errors in travel time variation.

192

193 **3.1. Calculation of transfer function**

194 Transfer functions, which represent the subsurface structure, are obtained by the
195 deconvolution of the daily stacked data using the generated force of the ACROSS source.
196 We used the force theoretically calculated using the operation parameters of the ACROSS
197 source. Then, we calculated the daily transfer functions for the clockwise and counter-
198 clockwise rotations and synthesizes the transfer functions for both the vertical and
199 horizontal source excitations. Figure 3a–c shows the transfer functions in the time domain
200 for each component obtained by stacking all the available data. They are used as reference
201 transfer functions in the calculation of travel time variation, as described in the following
202 section. The transfer functions are labeled with the components of the receiver and source

203 excitation. For example, the vertical motion excited by the vertical and horizontal forces
204 are labeled as Uv and Uh, respectively. Nv, Nh, Ev, and Eh are the northward and eastward
205 motions excited by the vertical and horizontal forces, respectively. The direction of the
206 horizontal excitation is indicated by the black arrow in Figure 2. In our study, two
207 horizontal components at the seismic stations are linearly combined to produce a
208 horizontal component, whose orientation is parallel to that of the horizontal excitation at
209 the source. The component is labeled as Hh in the following section.
210

211 ## 3.2. Travel time variation of P and S wave

212 We calculated the daily variation in the travel time using the method described by Ikuta
213 et al. (2002). We also calculated a cross-spectrum for both the P and S waves, between
214 the transfer function recorded for each day and the reference transfer function, which is
215 shown in Figure 3. The travel time difference ΔT and its uncertainty δt are calculated
216 using the following equations:

$$\Delta T = \frac{1}{\sum_n A_n} \sum_n A_n \frac{\theta_n}{\omega_n} \tag{4}$$

$$\delta t = \sqrt{\frac{1}{\left(\sum_{j=0}^{M-1} A_j\right)^2} \sum_{m=0}^{M-1} {A_m}^2 \left(\frac{\sin^{-1}\left(\tilde{\sigma}_m / \left|\tilde{X}_m\right|\right)}{\omega_m}\right)^2} \quad (5)$$

where A_n is the square root of the amplitude of the cross-spectral density, θ_n is the phase difference from the reference, and ω_n is the angular frequency in the n-th frequency components. $\tilde{X}_m$ and $\tilde{\sigma}_m$ are the Fourier transforms of the transfer function and the noise at the m-th frequency, respectively. M is the number of frequency components of the ACROSS signal used. Note that equation (5) is corrected from the equation proposed by Ikuta et al. (2002). The uncertainties calculated by the corresponding equation in Ikuta et al. (2002) were revealed to be overestimated.

We selected the P and S waves by applying Hanning windows to the transfer functions, as shown in Figure 3 and Table 2. The position and length of the windows were determined so that both the initial arrival and the maximum amplitude of the P or S waves were included. We used the Uv component for the P waves and the Hh component for the S waves. The horizontal direction of the Hh component was determined to give the largest amplitude in the horizontal particle motion, as shown in Figure 3d-f. For the N.MKBH

230 station, however, we used the Eh component without synthesizing because the sensor
231 trouble in the NS component remarkably reduced the number of available days. We
232 decided to use the Eh component instead of Hh because the direction of the maximum
233 amplitude was almost in the east-west direction.

234

235 Table 2 The window range and components for P and S wave

	Window for P wave [s]	Window for S wave [s]	horizontal direction
NU.MIK	0 - 0.2	0.1 - 0.3	N49.1° E
N.THNH	0.7 - 1.0	1.3 - 1.6	N56.4° E
N.MKBH	1.2 - 1.5	2.2 - 2.5	-

236 This table shows windows for P and S waves shown in Figure 2 and horizontal direction
237 of Hh component.

238

4 Results and discussion

In this section, we show the results of our analysis and discuss the influence of rainfall on seismic velocity variations. We examined the dependence of V_P and V_S on the crack density and fluid saturation using the theoretical relation provided by O'Connell and Budiansky (1974). Considering the SNR that decays with distance, we stacked the data for 60 days for the N.THNH and N.MKBH stations instead of using 1-day stacked data, which was used for the NU.MIK station.

4.1. Temporal variation of travel time

The temporal variation and uncertainties in the travel time obtained in our calculation are shown in Figures 4a-c. In temporal variations, both short-term and long-term changes can be recognized. First, we describe the variations for NU.MIK, which is located closest to the source and the ground water measuring facilities. In Figure 4, the high precipitation period from April to September in 2018 is shown by orange lines, and the low precipitation periods from December 2017 to March 2018 and October 2018 to February 2019 are shown by blue lines. At NU.MIK, many short-term changes in the travel time

255 are seen as step-like delays, with a maximum step of approximately 0.3 ms, followed by
256 a gradual recovery. Comparing these changes to the precipitation data, we found that they
257 are preceded by rainfalls, and significant changes were seen in the high precipitation
258 season in the given year. The magnitude of this change was larger in the P wave than in
259 the S wave. The long-term variation was also larger for the P waves than for the S waves.
260 A large advance of P wave was observed in late June 2018, whereas a small long-term
261 change was observed in the S wave during this period. In contrast, in May 2018, a large
262 delay in the S wave and a small change in the P wave was observed. The magnitudes of
263 these changes were about 0.9 ms and 0.6 ms for the P and S waves. This is notable
264 considering the overall change during the whole period of about 1.2 ms and 0.7 ms for P
265 and S waves, respectively.

266 Figures 4 b and c show the temporal variation in the travel times at the N.THNH and
267 N.MKBH stations, where the source-receiver distance is much larger than that in the case
268 of NU.MIK. Because of the low SNR, a moving average of 60 days was applied for these
269 stations. A 60-day long window was shifted at one-day step and averaged data were
270 plotted at the middle of the period when the window was applied. The data were not

271 plotted if the data deficit within the window was longer than 20 days. In these plots, the
272 short-term variations were suppressed but larger variations could be seen for the P wave
273 (more than that seen for the S wave), even with the difference in the uncertainties between
274 the P and S waves taken into account.

275

276 **4.2. Temporal relationship between velocities of P and S waves (Vp and Vs,**
277 **respectively)**

278 Figures 5a–d show the relationship between the changes in the Vp and Vs. Figures 5a–
279 c show the plots for all the periods in Figures 4a–c. Figure 5d shows the representative
280 variation during the period of rainfall indicated by the orange bar in Figures 4a, d, and e.
281 The velocity change rates $\delta V/V$ were calculated from the travel time variation using the
282 equation: $\delta V/V = -\delta T/T$

283 where δT is the travel time variation and T was chosen as the travel time at the middle
284 of each time window shown in Figure 3, which almost corresponds to the part of
285 maximum amplitude. The orange and blue lines in Figure 5 correspond to those in Figure
286 4.

The velocity variation at NU.MIK (Figure 5a) is mainly composed of three trends: decrease of Vp with a small increase of Vs during the low precipitation period, decrease of Vs without a major change of Vp in the beginning of the period of high precipitation, and an increase in both Vp and Vs during the high precipitation period. The amplitude of variation was observed to be larger in Vp than in Vs for both the long and short-term variations. The N.THNH (Figure 5b) station shows a trend in which only the Vp variation predominates. A small positive correlation between Vp and Vs is observed in this plot. This is also the case for N.MKBH, except for the small negative correlation between the Vp and Vs.

Figure 5d shows the typical response of Vp and Vs to rainfall at NU.MIK, corresponding to the period shown by the orange bar (June 19–July 4, 2018) in Figure 4. The travel times of both the P and S waves changed as a response to rainfall, as seen in Figure 4, but their responses were different. In the P wave, a sharp bend appears in the rainfall response, whereas the S wave shows a blunt bend. The rainfall-relevant change can be divided into three parts, as seen in Figure 5d: the Vp decreased immediately after the rainfall with a small decrease in the Vs; in the first half of the recovery response, the

303 Vp increases with a little change in the Vs; and in the second half, both Vp and Vs increase.
304 This type of temporal pattern is common for most of the responses to rainfalls observed
305 in NU.MIK.

306

307 **4.3. Influence of crack density and fluid saturation**

308 O'Connell and Budiansky (1974) theoretically calculated the Vp and Vs of a cracked
309 medium. They formulated the dependence of seismic velocity on the crack density and
310 fluid saturation and showed the difference between Vp and Vs. Figure 6 shows the
311 temporal variation of Vp and Vs obtained in our study plotted on the diagram using the
312 equations derived from O'Connell and Budiansky (1974). The base diagram shown in
313 Figure 6e indicates the change in Vp and Vs as a function of crack density and fluid
314 saturation (see Appendix). Note that Vp and Vs in these graphs represent the velocity
315 ratios with respect to an intact (crackless) medium. The dependence on fluid saturation
316 and crack density is different for Vp and Vs.

317 We interpreted the changes in Vp and Vs, which are shown in Figure 5, as shown in
318 Figure 6. Although it is difficult to know the seismic velocity of the intact condition of

the country-rock through which the seismic wave propagates, we tried to interpret this by assuming the initial ratios of Vp and Vs with those of the intact medium to be 0.6. Once the initial ratio is assumed, we can convert the velocity variation on Vp-Vs surface onto crack density – fluid saturation surface. In this process we use the equation as follows

$$\begin{bmatrix} dV_P \\ dV_S \end{bmatrix} = \begin{bmatrix} \dfrac{\partial V_P}{\partial \varepsilon} & \dfrac{\partial V_P}{\partial \xi} \\ \dfrac{\partial V_S}{\partial \varepsilon} & \dfrac{\partial V_S}{\partial \xi} \end{bmatrix} \begin{bmatrix} d\varepsilon \\ d\xi \end{bmatrix} = J \begin{bmatrix} d\varepsilon \\ d\xi \end{bmatrix} \tag{6}$$

where, ε and ξ denotes crack density and fluid saturation, respectively. J is generally called Jacobian. In the conversion, J can be calculated for the given initial ratio to give $(d\varepsilon, d\xi)$ from (dV_P, dV_S) using J^{-1}.

In the following sections, we show the changes in fluid saturation and crack density calculated from the changes in Vp and Vs, and examine whether we can infer the changes in the fluid saturation and crack density by monitoring Vp and Vs.

330 **4.4. Seasonal variation**

331 For all the stations, the observed variations of Vp and Vs almost fall on a linear trend,
332 in which fluid saturation and crack density have a positive correlation. This trend results
333 from the observation in which the variation in Vp is much larger than Vs.

334 In NU.MIK, the saturation and crack density decreased in the dry season. This may be
335 interpreted as a crack closure due to a decrease in the fluids in the cracks. The crack
336 density increased slightly at the beginning of the wet season, and both fluid saturation
337 and crack density increased in the following period. This may reflect fluid infiltration by
338 rainfall and the resultant crack openings. In contrast, N.THNH and N.MKBH showed
339 little difference between the dry and wet seasons. As these two stations were located
340 farther than NU.MIK from the ACROSS source, the P and S waves passed through the
341 deeper part of the crust. Therefore, it is expected that a contribution by the variation in
342 the deeper part, where small seasonal variation can be expected, for N.THNH and
343 N.MKBH is larger than for NU.MIK.

344

345 **4.5. Effects of short term rainfall**

346 As seen in the precipitation data observed by AMeDAS, the selected location
347 experiences heavy rainfalls every year. Therefore, it is interesting to discuss the temporal
348 response of Vp and Vs to a single rainfall event. Figure 6d shows the changing cycle
349 plotted on the diagram with the saturation and crack density for NU.MIK, corresponding
350 to Figure 5d. The changing cycle is composed of three stages, as explained in section 4.2.
351 In the first stage, just after rainfall, both saturation and crack density decreased
352 corresponding to the period when the Vp decreased (with a little change in the Vs). In the
353 second stage, both saturation and crack density increased corresponding to the period
354 when the Vp increased (with a small decrease in the Vs). In the third stage, saturation and
355 crack density continued to increase, with a larger increase in the saturation. This
356 interpretation seems strange because the fluid saturation may increase by rainfalls and
357 decrease after rainfalls. This incompatibleness will be discussed in the next section.

358

359 **4.6. Relation with change of ground water level**

360 We examined the relationship between the variations in the Vp and Vs and ground water

361 level measured by observational wells located near the ACROSS site, as shown in Figure
362 2. We tried to interpret the ground water level variation using the fluid saturation and
363 crack density, which are presumed by velocity changes, as stated in previous sections. As
364 shown in Figure 4d, TYH2 records short-term changes, such as rainfall response, whereas
365 TYH1 and TYE are insensitive to rainfall and may reflect the pressure of deeper aquifers.
366 Therefore, we use TYH2 for comparing the short-term changes. For comparison of long-
367 term variations, only TYH1 was used in this study because the records of TYH1 and TYE
368 were almost the same, and the long-term trend of TYH2 was similar to that of THY1. The
369 comparison was only made for NU.MIK because the observation well was located close
370 to the ACROSS source and NU.MIK.

371 The long-term variation of the Vp and Vs can be compared with the ground water level
372 of TYH1 (Figure 4d). Generally, the wet season corresponds to a period of high ground
373 water level. When the wet season starts, the groundwater level increases and stays high
374 until the dry season begins. In the period of high ground water level, the Vp gradually
375 increases (travel time decrease for P) with small variations in the Vs. The variation in the
376 seismic velocities in this period shows an increase in both the crack density and fluid

saturation of the subsurface rocks, which may indicate a continual diffusion of water in the ground. In the dry season, the ground water level decreases and the Vp decreases continually with a small change in the Vs. This indicates that the crack density and fluid saturation decrease with the water level. A clear decrease in the Vs (travel time increase of S) is observed in the period around the beginning of the wet season, from March to May of 2018. Taking into account the decrease in the Vp during this period, this change can be interpreted as an increase in the crack density and a small change in the saturation.

The short-term velocity change can be compared with the data of the shallower aquifer at TYH2. Though TYH2 sampled the water pressure at a depth of 130–150m, the aquifer was efficiently connected to the shallow part where the rain water could easily penetrate. In contrast to the long-term variation, the ground water level increased when the saturation and crack density decreases, as indicated by the decrease in the Vp.

However, the interpretation of crack density and water saturation, especially during the first stage of the rainfall, seems inconsistent with the groundwater observation. One possible explanation is the limited application of the study conducted by O'Connell and Budiansky (1974) with respect to the velocity response to rainfall. Mavko and Nolen-

393 Hoeksema (1994) discussed the effect of a gas–liquid mixture of pore fluid on the bulk
394 Vp using Gassmann's relation. In the case of the gas–liquid mixture, in fine scale and
395 within each crack, the bulk modulus of the gas–liquid mixture was almost equivalent to
396 that of gas even for a small amount of gas content, whereas the density increased as the
397 liquid content increased. Therefore, the bulk Vp decreased because of the density increase
398 without a change in the bulk modulus. The relation in O'Connell and Budiansky (1974)
399 does not take this into account but treats the fluid saturation as a ratio of saturated cracks
400 to the total number of cracks.

401 In the initial stage of the rainfall, the water infiltrates the ground, thereby increasing the
402 water content in each crack in the shallow subsurface. This may increase the density of
403 the medium without changing the bulk modulus, causing a decrease in both the Vp and
404 Vs. In the later stages, the Vp increased due to the decreasing water as indicated by the
405 ground water level.

406

407 5 Conclusion

408 We analyzed the travel time variations of both the P and S waves using a new type of

409 ACROSS vibration source that efficiently excited both the P and S waves. As a result of
410 the analysis, the annual variation and short-term changes, which resulted from water
411 infiltration in the ground, could be recognized. The variation in the Vp was larger than
412 that of Vs at all observation stations. The observed variations of Vp and Vs were then
413 converted to the variations in the crack density and fluid saturation of subsurface rocks
414 using the relation described by O'Connell and Budiansky (1974). By comparing the
415 velocity variations with the ground water level observed near the source, we found that
416 the seasonal variations in the ground water were consistent with the interpretation of fluid
417 saturation and crack density; however, the short-term variations associated with rainfall
418 events were inconsistent. This may be interpreted as an air-liquid mixture of fluid in
419 individual cracks.

420

421 # Declarations

422 **Ethics approval and consent to participate:** Not applicable

423 **Consent for publication:** Not applicable

List of abbreviations:

Accurately-controlled routinely-operated signal system: ACROSS

Signal-to-noise ratio: SNR

Velocity of P wave: Vp

Velocity of S wave: Vs

Automated meteorological data acquisition system: AMeDAS

National Institute of Advanced Industrial Science and Technology: AIST

Frequency modulations: FM

Vertical motion excited by the vertical and horizontal forces: Uv and Uh, respectively

Horizontal component, whose orientation is parallel to that of the horizontal excitation at the source: Hh

Availability of data and materials

The observed seismic data of Hi-net were obtained from the NIED website (https://doi.org/10.17598/NIED.0003).

Seismic data at NU.MIK were obtained from the NIED website (https://hinetwww11.bosai.go.jp/auth/?LANG=en).

Precipitation data were obtained from the JMA website (http://www.data.jma.go.jp/gmd/risk/obsdl/index.php).

Groundwater level data were provided by the Tectonic-Hydrology Group, Research Institute of Earthquake and Volcano Geology (IEVG), and National Institute of Advanced Industrial Science and Technology (AIST) on request.

Map data was obtained from the GSI maps from the website of the Geospatial Information Authority of Japan (https://maps.gsi.go.jp).

Competing interests

The authors declare no competing interests.

Funding

This study was supported by the Nagoya University and the project on Earthquake and Volcano Hazards Observation and Research Program.

Authors' contributions

RS performed the analysis and wrote the draft of the manuscript, KY supervised RS for implementing the analysis method and its interpretation, and ST and TW maintained the monitoring system of the ACROSS and discussed the interpretation.

Acknowledgements

We used the seismic data provided by the National Research Institute for Earth Science and Disaster Resilience, Graduate School of Environmental Studies, and Nagoya University. The data were automatically acquired and stacked in Nagoya University. The meteorological data were provided by the Japan Meteorological Agency. The ground water data were provided by the National Institute of Advanced Industrial Science and Technology. The map data were provided by the Geospatial Information Authority of Japan.

References

Brenguier F, Campillo M, Hadziioannou C, Shapiro NM, Nadeau RM, Larose E (2008) Postseismic

relaxation along the San Andreas fault at Parkfield from continuous seismological observations. Science 321:1478–1481. https://doi.org/10.1126/science.1160943

Clements T, Denolle MA (2018) Tracking groundwater levels using the ambient seismic field. Geophys Res Lett 45:6459–6465. https://doi.org/10.1029/2018GL077706

Grêt A, Snieder R, Scales J (2006) Time-lapse monitoring of rock properties with coda wave interferometry. J Geophys Res 111:n/a–n/a. https://doi.org/10.1029/2004JB003354

Hobiger M, Wegler U, Shiomi K, Nakahara H (2016) Coseismic and post-seismic velocity changes detected by Passive Image Interferometry: comparison of one great and five strong earthquakes in Japan. Geophys J Int 205:1053–1073. https://doi.org/10.1093/gji/ggw066

Ikuta R, Yamaoka K (2004) Temporal variation in the shear wave anisotropy detected using the Accurately Controlled Routinely Operated Signal System (ACROSS). J Geophys Res 109:n/a–n/a. https://doi.org/10.1029/2003JB002901

Ikuta R, Yamaoka K, Miyakawa K, Kunitomo T, Kumazawa M (2002) Continuous monitoring of propagation velocity of seismic wave using ACROSS. Geophys Res Lett 29:3–6. https://doi.org/10.1029/2001GL013974

Karageorgi E, Clymer R, McEvilly TV (1992) Seismological studied at Parkfield. Ⅱ. Search for temporal variations in wave propagation using vibroseis. Bull Seismol Soc Am 82:1388–1415

Kasahara J, Hasada Y (2016) Time lapse approach to monitoring oil, gas, and CO_2 storage by seismic methods. Amsterdam: Gulf Professional Publishing. 15–34

King MS, Marsden JR, Dennis JW (2000) Biot dispersion for P- and S-wave velocities in partially and fully saturated sandstones. Geophys Prospect 48:1075–1089. https://doi.org/10.1111/j.1365-2478.2000.00221.x

Kunitomo T (2014) An improvement in the precision of measuring seismic travel time changes with the use of the hi-net data. Zisin 66:97–112. https://doi.org/10.4294/zisin.66.97 (in Japanese)

Liu Z, Huang J, Peng Z, Su J (2014) Seismic velocity changes in the epicentral region of the 2008 Wenchuan earthquake measured from three-component ambient noise correlation techniques. Geophys Res Lett 41:37–42. https://doi.org/10.1002/2013GL058682

Maeda Y, Yamaoka K, Miyamachi H, Watanabe T, Kunitomo T, Ikuta R, Yakiwara H, Iguchi M (2015) A subsurface structure change associated with the eruptive activity at Sakurajima Volcano, Japan, inferred from an accurately controlled source. Geophys Res Lett 42:5179–5186. https://doi.org/10.1002/2015GL064351

499 Martini F, Bean CJ, Saccorotti G, Viveiros F, Wallenstein N (2009) Seasonal cycles of seismic velocity
500 variations detected using coda wave interferometry at Fogo volcano, São Miguel, Azores, during
501 2003–2004. J Volcanol Geotherm Res 181:231–246.
502 https://doi.org/10.1016/j.jvolgeores.2009.01.015
503 Matsumoto N, Kitagawa Y, Koizumi N (2007) Groundwater-level anomalies associated with a
504 hypothetical preslip prior to the anticipated Tokai earthquake: detectability using the groundwater
505 observation network of the geological survey of Japan, AIST. Pure Appl Geophys 164:2377–2396.
506 https://doi.org/10.1007/s00024-007-0278-4
507 Mavko G, Nolen-Hoeksema R (1994) Estimating seismic velocities at ultrasonic frequencies in partially
508 saturated rocks. Geophysics 59:252–258. https://doi.org/10.1190/1.1443587
509 Miao Y, Shi Y, Wang SY (2018) Temporal change of near-surface shear wave velocity associated with
510 rainfall in Northeast Honshu, Japan. Earth Planets and Space 70–1. https://doi.org/10.1186/s40623-
511 018-0969-3
512 Nagao H, Nakajima T, Kumazawa M, Kunitomo T (2010) Stacking strategy for acquisition of an
513 ACROSS transfer function. In: Handb Geophys Explor Seismic Explor. Pergamon:213–227
514 Nakata N, Snieder R (2011) Near - surface weakening in Japan after the 2011 Tohoku - Oki

515 earthquake. Geophys Res Lett 38:n/a–n/a. https://doi.org/10.1029/2011GL048800

516 National Research Institute for Earth Science and Disaster Resilience (2019)

517 NIED Hi-net, National Research Institute for Earth Science and Disaster Resilience.

518 https://doi.org/10.17598/NIED.0003

519 Niu F, Silver PG, Daley TM, Cheng X, Majer EL (2008) Preseismic velocity changes observed from

520 active source monitoring at the Parkfield SAFOD drill site. Nature 454:204–208.

521 https://doi.org/10.1038/nature07111

522 Nur A, Simmons G (1969) The effect of saturation on velocity in low porosity rocks. Earth Planet Sci Lett

523 7:183–193. https://doi.org/10.1016/0012-821X(69)90035-1

524 O'Connell RJ, Budiansky B (1974) Seismic velocities in dry and saturated cracked solids. J Geophys Res

525 79:5412–5426. https://doi.org/10.1029/JB079i035p05412

526 Richter T, Sens-Schönfelder C, Kind R, Asch G (2014) Comprehensive observation and modeling of

527 earthquake and temperature-related seismic velocity changes in northern Chile with passive image

528 interferometry. J Geophys Res Solid Earth 119:4747–4765. https://doi.org/10.1002/2013JB010695

529 Saiga A, Yamaoka K, Kunitomo T, Watanabe T (2006) Continuous observation of seismic wave velocity

and apparent velocity using a precise seismic array and ACROSS seismic source. Earth, Planets and Space 58:993–1005. https://doi.org/10.1186/BF03352604

Sens-Schönfelder C, Wegler U (2006) Passive image interferometry and seasonal variations of seismic velocities at Merapi Volcano, Indonesia. Geophys Res Lett 33. https://doi.org/10.1029/2006GL027797

Silver PG, Daley TM, Niu F, Majer EL (2007) Active source monitoring of cross-well seismic travel time for stress-induced changes. Bull Seismol Soc Am 97:281–293. https://doi.org/10.1785/0120060120

Tsuji S, Yamaoka K, Ikuta R, Kunitomo T, Watanabe T, Yoshida Y (2018) Secular and coseismic changes in S - wave velocity detected using ACROSS in the Tokai region. Earth Planets and Space. https://doi.org/10.1186/s40623-018-0917-2

Wang B, Yang W, Wang W, Yang J, Li X (2020) Diurnal and semidiurnal P - and S - wave velocity changes measured using an air gun source. Journal of Geophysical Research: Solid Earth. https://doi.org/10.1029/2019JB018218

Wegler U, Lühr B-G, Snieder R, Ratdomopurbo A (2006) Increase of shear wave velocity before the 1998 eruption of Merapi volcano (Indonesia). Geophys Res Lett 33:4–7. https://doi.org/10.1029/2006GL025928

546 Yamamura K, Sano O, Utada H, Takei Y, Nakao S, Fukao Y (2003) Long-term observation of in situ
547 seismic velocity and attenuation. J Geophys Res 108:1–15. https://doi.org/10.1029/2002JB002005
548 Yamaoka K, Kunitomo T, Miyakawa K, Kobayashi K, Kumazawa M (2001) A trial for monitoring
549 temporal variation of seismic velocity using an ACROSS system. Isl Arc 10:336–347.
550 https://doi.org/10.1046/j.1440-1738.2001.00332.x

551 .

552 **Figure legends**

553 Figure 1. Photograph of ACROSS source used in this study. Eccentric weights rotate
554 around a horizontal axis to produce a sinusoidal signal. Both horizontal and vertical
555 forces generated by the rotation develop efficient excitations of P and S waves

556

557 Figure 2. Locations of ACROSS source and observation stations. Red circle and blue
558 squares indicate the locations of the ACROSS source and seismic stations, respectively.
559 Yellow triangles denote AMeDAS stations used for rainfall measurements. The ground
560 water observation wells are shown as orange circles. The black arrow indicates the

561 direction of horizontal vibration of ACROSS source. Map data are provided by the

562 Geospatial Information Authority of Japan

563

564 Figure 3. Transfer functions obtained by stacking of all available data o. Figures (a) to

565 (c) show the transfer functions obtained by stacking all available daily transfer

566 functions. Orange and green bars show the range of windows applied to extract P wave

567 and S wave, respectively. (d) to (f) indicate particle motions of the S wave extracted

568 form Nh and Eh component shown on a horizontal plane. Triangle and rectangle marks

569 indicate beginning and end of the motion in the time window, respectively

570

571 Figure 4. Temporal variations of travel time, ground water levels, and rainfalls.

572 Figures (a) to (c) show travel time variations of P and S waves. Solid and dotted lines

573 show the P and S wave, respectively. The width between two horizontal bars in the right

574 of each figure indicate the estimation errors of P wave (left) and S wave (right). (d)

575 shows daily variation of ground water level at TYH1 (solid line), TYH2 (dotted line),

576 and TYE (dash-dotted line). (e) and (f) show daily rainfall observed at Toyohashi and

577 Mikkabi stations, respectively. Orange lines show high precipitation period (wet season)
578 from April to September in 2018; blue lines show low precipitation period (dry season).
579 Areas painted by orange bars in (a), (d), and (e) show the periods used in analysis for
580 short-term travel time change

581

582 Figure 5. Relation between temporal changes of Vp and Vs. Figures (a), (b) and (c)
583 show the variation of Vp and Vs during the observation period at NU.MIK, N.THNH,
584 and N.MKBH, respectively. Blue lines indicate variation during low precipitation
585 period; orange lines show variation during high precipitation period indicated in Figure
586 4. (d) shows short-term velocity change associated with rainfall indicated in Figure 4 for
587 NU.MIK. Circle and triangle marks indicate the beginning and end of the period

588

589 Figure 6. Temporal variation of crack density and fluid saturation converted from Vp
590 and Vs Variations of Vp and Vs are converted into those of crack density and fluid
591 saturation as per O'Connell and Budiansky (1974). (e) Based on the results, variations
592 of Vp and Vs are shown as a function of crack density and saturation. The green and

593 yellow lines show Vp and Vs as a ratio to intact medium, respectively. (a), (b), and (c)

594 show the variations at NU.MIK, N.THNH, and N.MKBH, respectively. (d) shows the

595 short-term change associated with rainfall at NU.MIK. The rectangle in (e) shows the

596 plotted area shown in (a–d)

597

Figures

Figure 1

Photograph of ACROSS source used in this study. Eccentric weights rotate around a horizontal axis to produce a sinusoidal signal. Both horizontal and vertical forces generated by the rotation develop efficient excitations of P and S waves

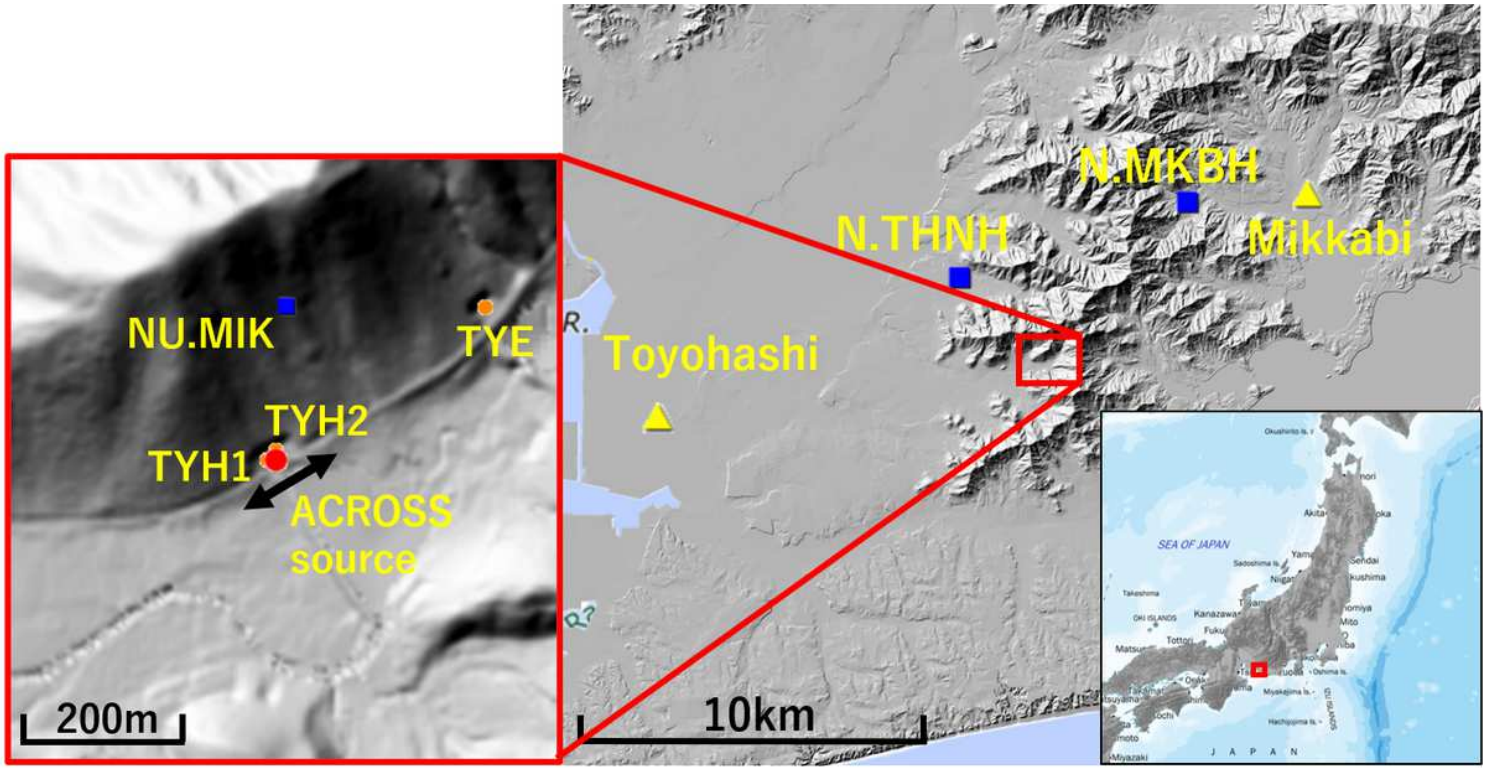

Figure 2

Locations of ACROSS source and observation stations. Red circle and blue squares indicate the locations of the ACROSS source and seismic stations, respectively. Yellow triangles denote AMeDAS stations used for rainfall measurements. The ground water observation wells are shown as orange circles. The black arrow indicates the direction of horizontal vibration of ACROSS source. Map data are provided by the Geospatial Information Authority of Japan

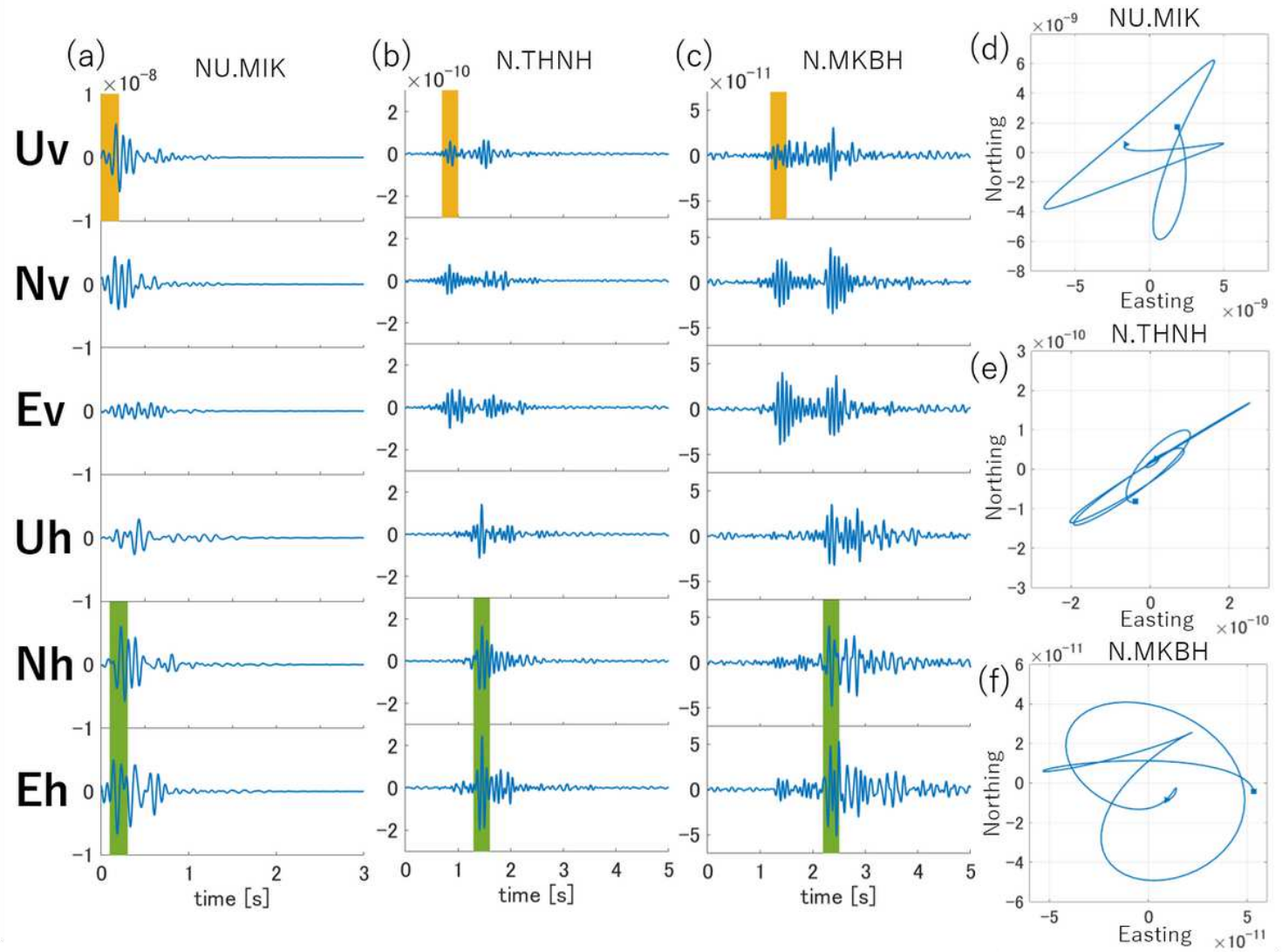

Figure 3

Transfer functions obtained by stacking of all available data o. Figures (a) to (c) show the transfer functions obtained by stacking all available daily transfer functions. Orange and green bars show the range of windows applied to extract P wave and S wave, respectively. (d) to (f) indicate particle motions of the S wave extracted form Nh and Eh component shown on a horizontal plane. Triangle and rectangle marks indicate beginning and end of the motion in the time window, respectively

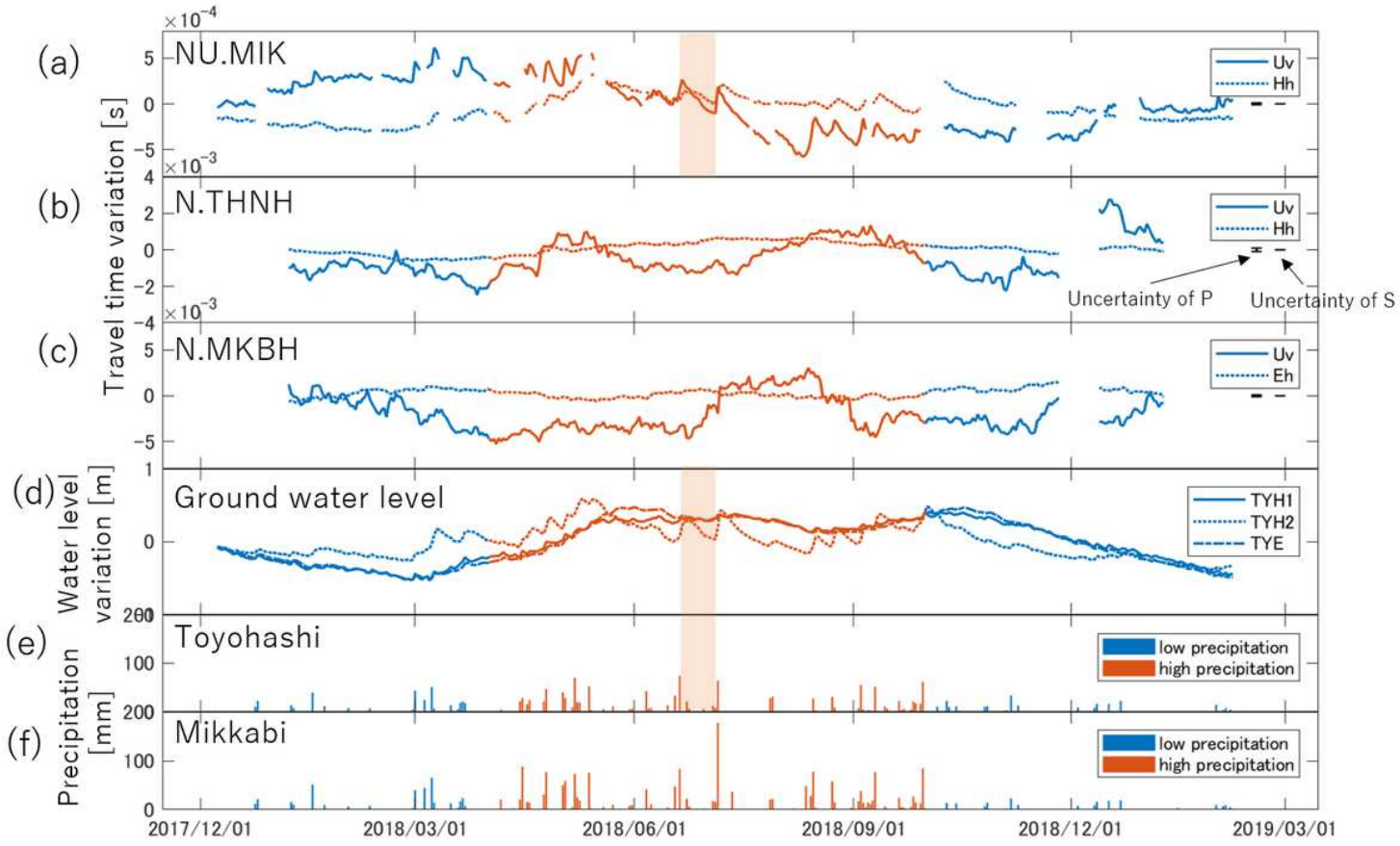

Figure 4

Temporal variations of travel time, ground water levels, and rainfalls. Figures (a) to (c) show travel time variations of P and S waves. Solid and dotted lines show the P and S wave, respectively. The width between two horizontal bars in the right of each figure indicate the estimation errors of P wave (left) and S wave (right). (d) shows daily variation of ground water level at TYH1 (solid line), TYH2 (dotted line), and TYE (dash-dotted line). (e) and (f) show daily rainfall observed at Toyohashi and Mikkabi stations, respectively. Orange lines show high precipitation period (wet season) from April to September in 2018; blue lines show low precipitation period (dry season). Areas painted by orange bars in (a), (d), and (e) show the periods used in analysis for short-term travel time change

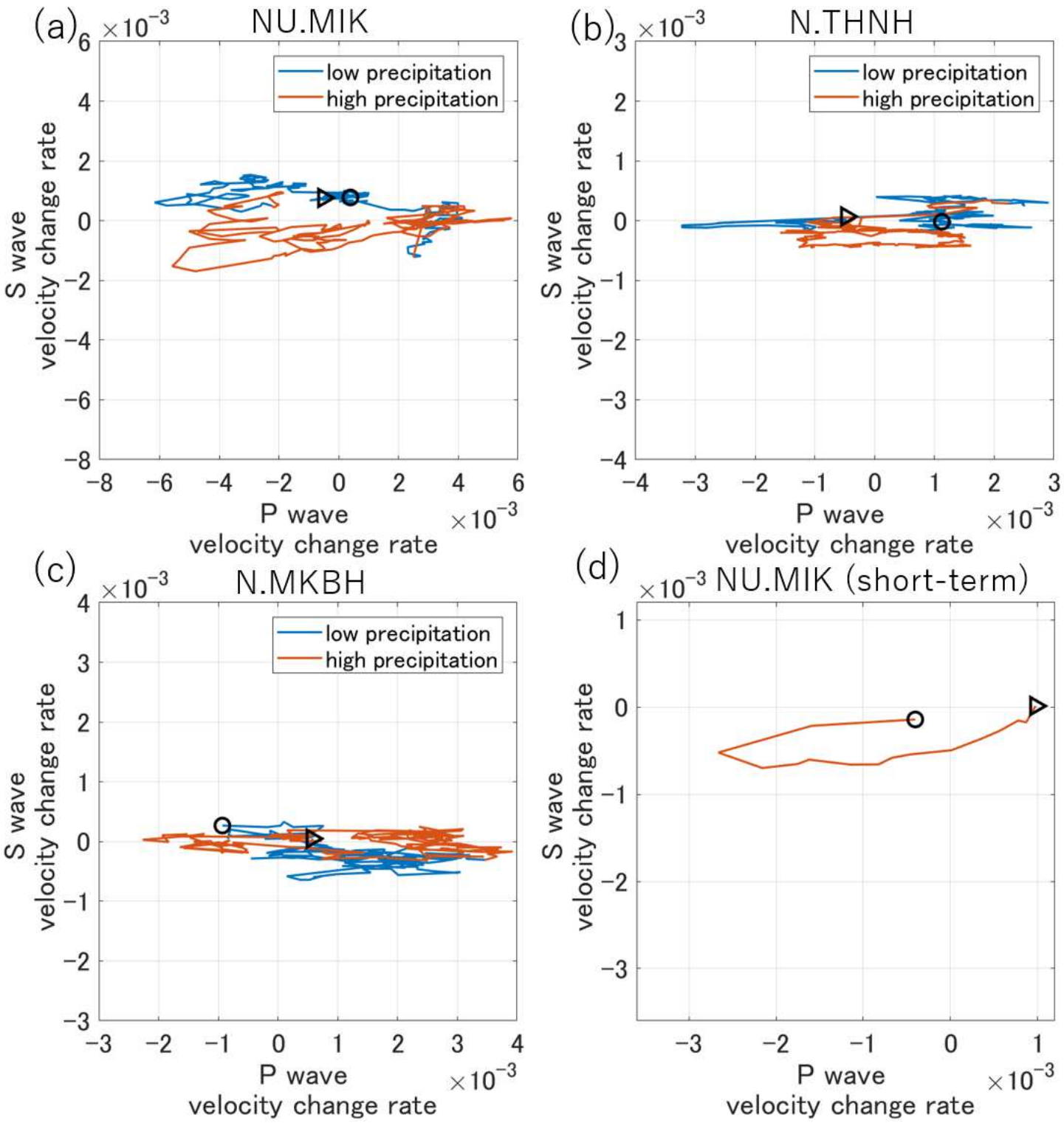

Figure 5

Relation between temporal changes of Vp and Vs. Figures (a), (b) and (c) show the variation of Vp and Vs during the observation period at NU.MIK, N.THNH, and N.MKBH, respectively. Blue lines indicate variation during low precipitation period; orange lines show variation during high precipitation period indicated in Figure 4. (d) shows short-term velocity change associated with rainfall indicated in Figure 4 for NU.MIK. Circle and triangle marks indicate the beginning and end of the period

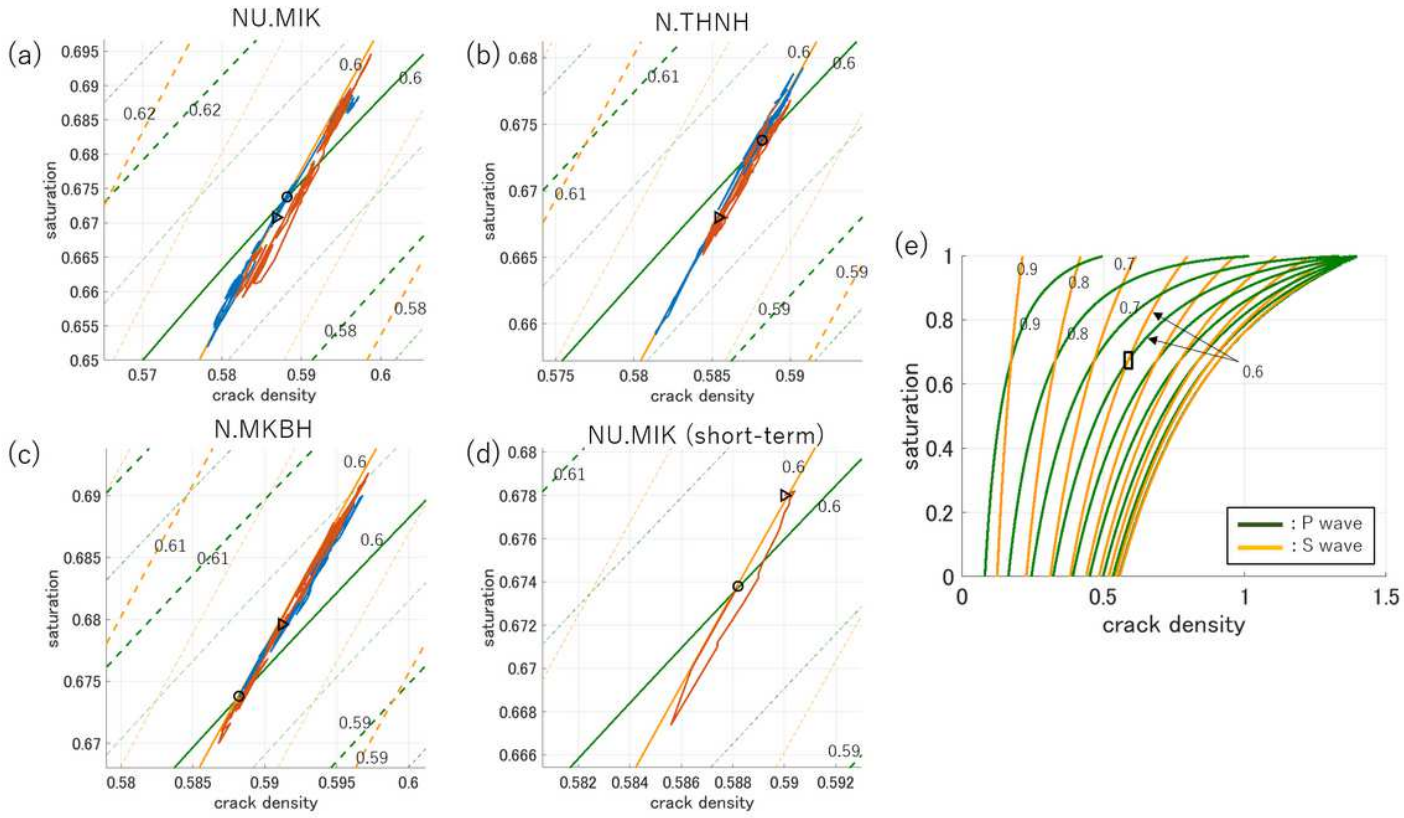

Figure 6

Temporal variation of crack density and fluid saturation converted from Vp and Vs Variations of Vp and Vs are converted into those of crack density and fluid saturation as per O'Connell and Budiansky (1974). (e) Based on the results, variations of Vp and Vs are shown as a function of crack density and saturation. The green and yellow lines show Vp and Vs as a ratio to intact medium, respectively. (a), (b), and (c) show the variations at NU.MIK, N.THNH, and N.MKBH, respectively. (d) shows the short-term change associated with rainfall at NU.MIK. The rectangle in (e) shows the plotted area shown in (a–d)

Supplementary Files

This is a list of supplementary files associated with this preprint. Click to download.

- Appendix.docx
- GraphicalAbstract.png